Trapping plasmonic nanoparticles with MHz electric fields

Filippos Harlaftis, Dean Kos, Qianqi Lin, et al.

View Online   Export Citation   CrossMark

Trapping plasmonic nanoparticles with MHz electric fields

View Online   Export Citation   CrossMark

Filippos Harlaftis, Dean Kos, Qianqi Lin,[a] Kevin T. P. Lim, Calvin Dumesnil, and Jeremy J. Baumberg[a]

AFFILIATIONS

Nanophotonics Centre, Department of Physics, Cavendish Laboratory, University of Cambridge, Cambridge CB3 0HE, England, United Kingdom

[a]Authors to whom correspondence should be addressed: ql285@cam.ac.uk and jjb12@cam.ac.uk

ABSTRACT

Dielectrophoresis drives the motion of nanoparticles through the interaction of their induced dipoles with a non-uniform electric field. We experimentally observe rf dielectrophoresis on 100 nm diameter gold nanoparticles in a solution and show that for MHz frequencies, the nanoparticles can reversibly aggregate at electrode gaps. A frequency resonance is observed at which reversible trapping of gold nanoparticle "clouds" occurs in the gap center, producing almost a 1000-fold increase in density. Through accounting for gold cores surrounded by a conducting double layer ion shell, a simple model accounts for this reversibility. This suggests that substantial control over nanoparticle separation is possible, enabling the formation of equilibrium nanoarchitectures in specific locations.

Dielectrophoresis (DEP) drives particles in suspension under the influence of polarization forces from inhomogeneous electric fields and is of increasing interest for biological applications and nano- and micro-fabrication.[1–3] DEP can be used to form chains of nanostructures such as gold nanoparticles (AuNPs) for their integration into electrically functional nanodevices,[4–7] chemiresistors,[8] and plasmonic sensors.[9,10] Understanding of DEP fundamentals and phenomena accounts for effects of electrode geometry, electrolyte, particle size, temperature, frequency, voltage, and particle composition.[4,5,11–13]

However, despite this, manipulation of such AuNPs without irreversibly fixing them into chain-like structures is scarce. Here, we show resonant trapping of colloidal nanoparticles into dense clouds within an electrode gap that can be released and retrapped on sub-second timescales. A few previous instances of reversible assembly[14–16] (working in different conditions to here) offer only preliminary explanation of assembly mechanisms, poor control of morphology, and with no MHz resonances observed. Here, we find that trapping can be explained by the balance among electrostatic repulsion, Brownian motion, and DEP forces under low fluid velocity. We explore this process electrically, optically, and spectroscopically to systematically identify the conditions and mechanisms for NP trapping.

For spherical nanoparticles (radius R), the induced dipole moment depends linearly on external electric field E in medium ε_m, the dielectrophoretic potential[17] is

$$U_{\text{DEP}} = -2\pi\varepsilon_m R^3 \text{Re}(K) |\overline{E}|_{\text{rms}}^2 \quad (1)$$

with force $\overline{F} = -\nabla U_{\text{DEP}}$. This force depends linearly on the particle volume and the field density gradient. The Clausius–Mossotti parameter $\text{Re}(K)$ depends on frequency, offering subtle control of the DEP force, as we show below.

A flow cell geometry is adopted to give both optical access and electrical driving through an array of electrode pairs with triangular tips (to give the highest field gradients for trapping). These electrode sets are spaced 4 mm apart and contacted by external probes on pads [Figs. 1(a)–1(c)]. Electrode gap sizes of 8 μm are shown, though similar results are obtained for a range of gaps. A polydimethylsiloxane (PDMS) microfluidic chip placed on top has chambers separately enclosing each electrode pair and isolating each gap [Figs. 1(d) and 1(g)]. Isolation is important to avoid interactions, contamination, and NP deposition onto neighboring electrodes. Holes are punched through the PDMS to attach tubing and flow NP solutions through the chambers [Fig. 1(d)]. Electrodes of 50 nm thick Au on 5 nm Cr are produced by laser lithography and standard liftoff. An rf function generator feeds an amplifier (Mini-circuits ZX60-100VH+) with matched 50 Ω load, and both the gap driving voltage V_P and current $V_s/50$ Ω are recorded using a pre-amplifier (Femto HVA-10M-60-F) and a lock-in amplifier (SR844 Stanford Research Systems) [Fig. 1(e)].
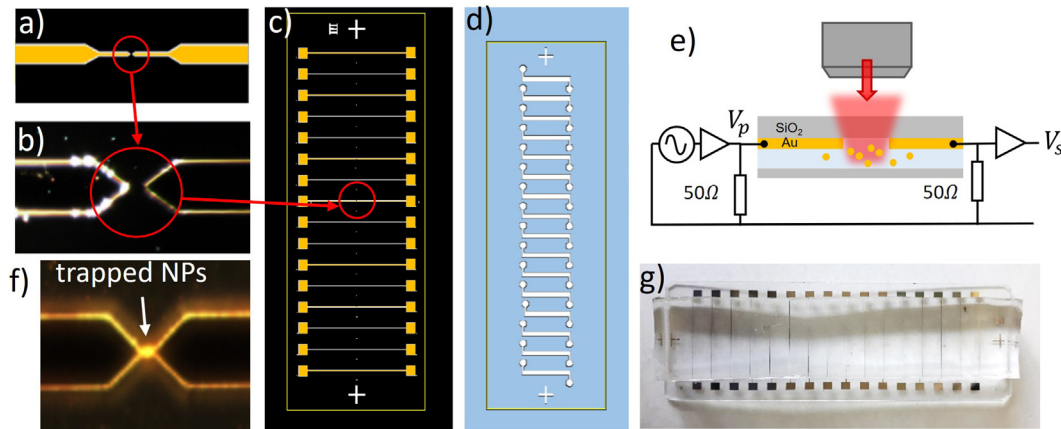
FIG. 1. Electrode geometry showing (a) electrode design and (b) a dark-field image of 8 μm gap. (c) Electrode array and (d) PDMS microfluidic chamber layouts. (e) Experiment setup that (f) traps NPs at 3 MHz, using (g) fabricated sample with upper PDMS microfluidic chambers.

The experiments are performed across a range of potential amplitudes ($V_p = 1$–20 V) at various frequencies. At lower frequencies (10–500 kHz), strong AC electroosmotic and/or electrothermal fluid flows are observed around the contacts, which sweep away any NP clouds and thus need to be avoided. However, at higher frequencies, the AuNPs can be released and subsequently diffuse after switching off the voltage (Fig. 2). At these higher frequencies (1–5 MHz), scattering intensities scale near-quadratically with voltage as expected for the dielectrophoretic force [see Eq. (1)].

Applying MHz sinusoidal potentials of amplitude $V_p = 20$ V (pk to pk), the 100 nm diameter AuNPs (BBI Solutions) are attracted toward the electrode gap and also gather near the sharp electrode edges. In specific situations, a bright AuNP aggregation (cloud) can be observed in the gap with the voltage on [Figs. 1(f) and 3(a)], which is released upon switching off. Trapping requires V_p to exceed a different value at each frequency [Fig. 2(e), arrows]. To systematically reproduce and understand AuNP-cloud formation, video images are collected in real time simultaneously with dark-field (DF) spectroscopy from the inner gap location. To quantify AuNP trapping, the voltage is periodically switched on and off, while the driving frequency is slowly increased from 0.5 to 5MHz [Figs. 3(b) and 3(c)].

For $V_p = 20$ V, as the frequency increases to 1.5–2 MHz, a dense AuNP cloud forms in the gap center, which slowly elongates and moves to the electrodes at higher frequencies [Fig. 3(a)]. High-angle illumination dark-field scattering is analyzed both for the total scattering intensity across the image [I_{DF} image, Fig. 3(e)] and from a sub-micrometer spot in the gap center, which is directed to a fiber-coupled spectrometer [I_{DF} cloud, Fig. 3(d)]. The latter gives DF spectra characteristic of 100 nm AuNPs (peaked around 580 nm) whose spectral shape is independent of the trapping conditions showing that in all cases here the NPs remain >50 nm apart (see below) so that significant optical coupling is not observed. The 50–100-fold enhanced scattering intensity compared to the surrounding solution away from the electrodes suggests that the initial 7 μm separation (given the 4×10^9 NPs/ml) is reduced to nearly 1 μm in the densest clouds.

Initially, after first turning the rf voltage on (green vertical lines), the AuNP density increases over $\tau \sim 30$ s, subsequently increases more slowly, and eventually saturates. When the rf voltage is then
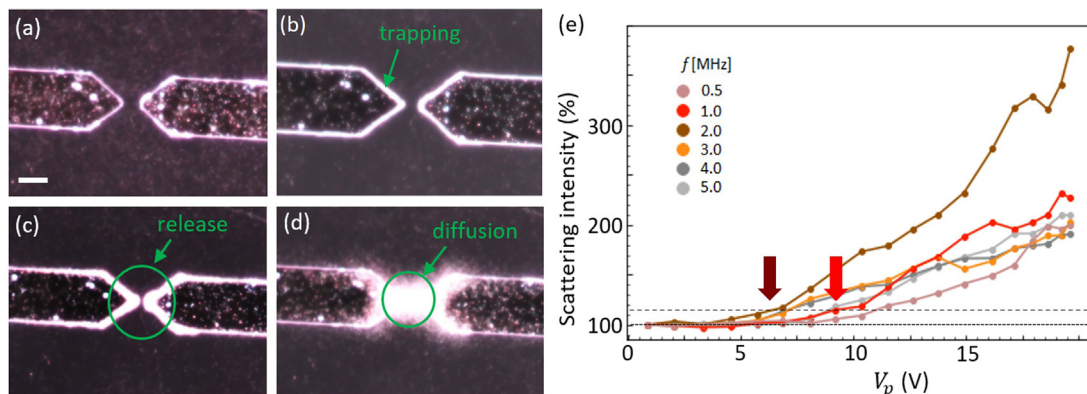
FIG. 2. Dark-field images: (a) before voltage applied, (b) upon trapping at electrode edges with voltage on (after 90 s), (c) initially when the voltage turned off (100 ms), and (d) after a further 3 s showing diffusion of AuNPs away from electrodes. Scale bar is 10 μm. (e) Scattering strength from gap vs rf voltage, arrows show intensity at which scattering from cloud trapping increases by >15% (dashed line) at 1 and 2 MHz.
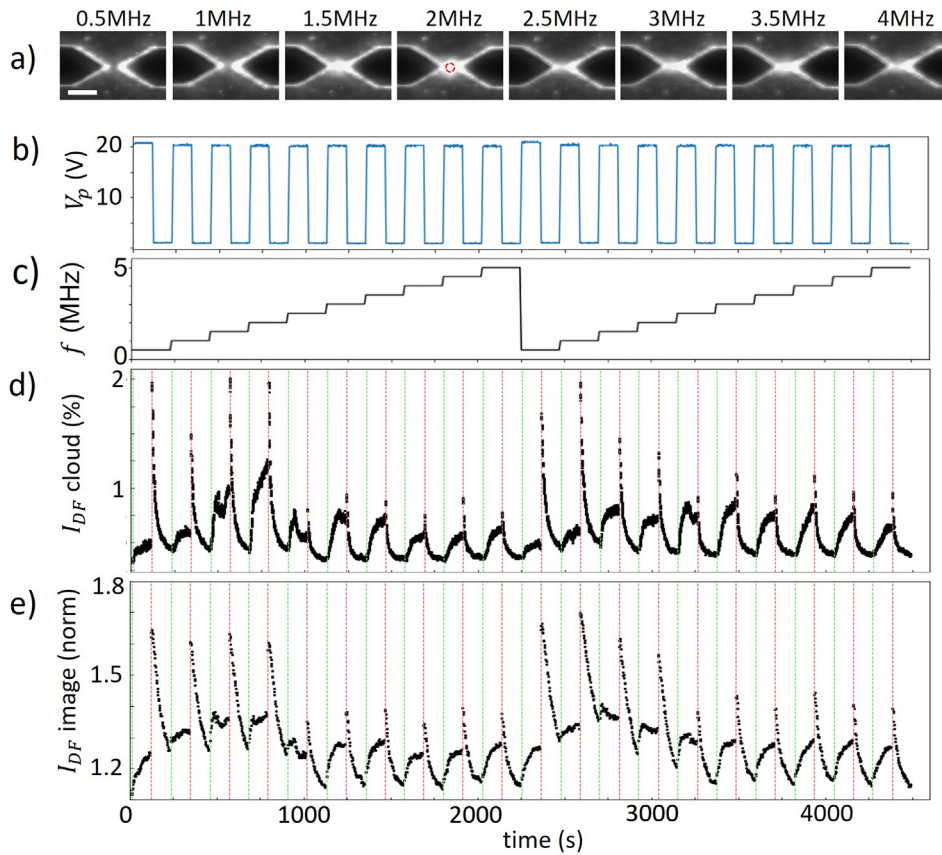
FIG. 3. (a) Images of the electrode gap at increasing rf frequency and $V_p = 20$ V showing trapping of AuNPs in the gap center, scale bar 10 μm. (b) Applied voltage and (c) frequency vs time, resolving (d) dark-field scattered intensity at $\lambda = 600$ nm at the gap center [within red circle in (a)] and (e) average integrated dark-field image intensity in the region around the gap.

turned off (red vertical lines), sharp intensity spikes are seen within 300 ms, which exponentially decay in 10 s from the gap center [Fig. 3(d)] and 60 s from the wider gap region [Fig. 3(e)]. These spikes exist whether or not a AuNP cloud forms and are due to trapping of additional AuNPs in the vicinity of the electrode edges (Fig. 2), which are also released when the voltage is turned off. The 100 nm AuNPs should diffuse 10 μm in 6 s, similar to that observed when they expand through the gap region. However, the fast sub-second rise on initial turn-off suggests a ballistic expulsion from the electrode edges.

The AuNP cloud trapping shows a resonant frequency response in both spectra and images with maximum scattering at ~ 2 MHz (see non-spike increases in Fig. 3). The exact AuNP cloud density corresponding to the enhanced light scattering depends on the history of each electrode pair (likely because deposited NPs on the contacts change the field gradients). This can be seen in the second scan in Fig. 2, which shows slightly different response although the same general resonance. Typically however, a stable trap is always formed, which attracts AuNPs from a wide volume into the gap up to a saturation density set by the interparticle forces. In contrast to this stable reversible trapping, at lower frequencies ($\sim$10 kHz) and lower voltages ($V_p < 10$ V), the AuNPs become permanently attached to the electrodes, leading to the formation of microwires as previously reported.[4,6,11,18] This indicates that the shape of the interparticle potential strongly changes with frequency.

To model the trapping, we combine DEP with the Derjaguin–Landau–Verwey–Overbeek (DVLO) theory of colloidal forces[19,20] that balances van der Waals attraction U_{VdW} with the electrostatic repulsion U_{elec} of the negatively charged particles ($\zeta \sim -54$ meV for these 100 nm citrate-coated BBI AuNPs)

$$U_{tot} = U_{VdW} + U_{elec} + U_{DEP},$$

$$U_{VdW} = -\frac{A_H}{6}\left[\frac{R}{r} + \frac{R}{r+2R} + \ln\left(\frac{r}{r+2R}\right)\right], \quad (2)$$

$$U_{elec} = 4\pi\varepsilon_m R\zeta^2 \ln\left(1 + e^{-r/\lambda_D}\right), \quad (3)$$

with the Hamaker factor A_H for Au (which varies from 0.6 to 1.6 eV in the literature[19]), the Debye screening length from ions in the solution λ_D, permittivity of liquid medium ε_m, and separation of NP surfaces r. Assuming that ac electro-osmosis and electrothermal flows can be ignored (driving bulk liquid flows at low frequencies but invisible already in our experiments at 1 MHz), the frequency dependence emerges from Re(K). To further support this hypothesis, we note that the crossover frequency for AC electro-osmosis[11,21] is $\left[\frac{\pi}{2}\tau\frac{d}{\lambda_D}\right]^{-1} \simeq 0.1$ MHz (where $\tau \simeq 35$ ns is the charge relaxation time and $d \sim 1\,\mu$m is the characteristic dimension of the system). This is an order of magnitude lower than the resonant frequencies found here. In contrast, the crossover frequency for electrothermal flows[16,22] is $1/(2\pi\tau) \cong 4.5$ MHz, around those studied here. Previous work analyzing the frequency dependence of electrothermal flows in more detail shows crossover frequencies between 0.1 and 10 MHz.[11,22] Electrothermal flows are proportional to the

temperature gradient that is established from heat sources such as Joule heating or microscope light absorption.[16] Despite this, we observe no flows above 1 MHz, possibly because the small vertical dimension of our microchamber (60 μm) relative to the characteristic system dimensions (~1 μm) makes temperature gradients small.[16] To estimate Re(K) for a bare AuNP (real permittivity Re[ε_p] ~ $-10^4 \varepsilon_0$, conductivity σ_p ~ $10^{11} \mu$S/cm) in the low conductivity water medium ($\varepsilon_m \simeq 79\varepsilon_0$, σ_m ~ 200μS/cm, where conductivity is directly measured with a Zetasizer Nano, Malvern Panalytical), we have

$$\mathrm{Re}(K) \simeq \frac{\sigma_p - \sigma_m}{\sigma_p + 2\sigma_m} = 1 \quad (\omega < \omega_{MW} = 1/\tau_{MW} = 10^{14} \text{ MHz}),$$

which is not frequency dependent and is inconsistent with the experimental data. Here, ω_{MW} is the relaxation frequency due to Maxwell–Wagner polarization, which sets the transition frequency for Re(K).

To elicit a MHz frequency resonance, this model has to be modified with a shell of thickness δ [Fig. 4(a)], consistent with the double-layer around AuNPs in a solution due to bound surface citrate anions interacting with dissolved ions. This model results in a composite effective particle permittivity[23]

$$\tilde{\varepsilon}'_p = \tilde{\varepsilon}_s \left[\frac{(1 + \delta/r)^3 + 2K_{ps}}{(1 + \delta/r)^3 - K_{ps}} \right],$$

where $K_{ps} = \frac{\tilde{\varepsilon}_p - \tilde{\varepsilon}_s}{\tilde{\varepsilon}_p + 2\tilde{\varepsilon}_s}$.

Assuming $\varepsilon_s \leq \varepsilon_m \ll |\varepsilon_p|$ and $\sigma_s \ll \sigma_p$, this implies $K_{ps} \sim 1$, so that $\tilde{\varepsilon}'_p = h\tilde{\varepsilon}_s$ with $h = 1 + 3/[(1 + \delta/R)^3 - 1]$, and resulting in the effective Clausius–Mossotti parameter
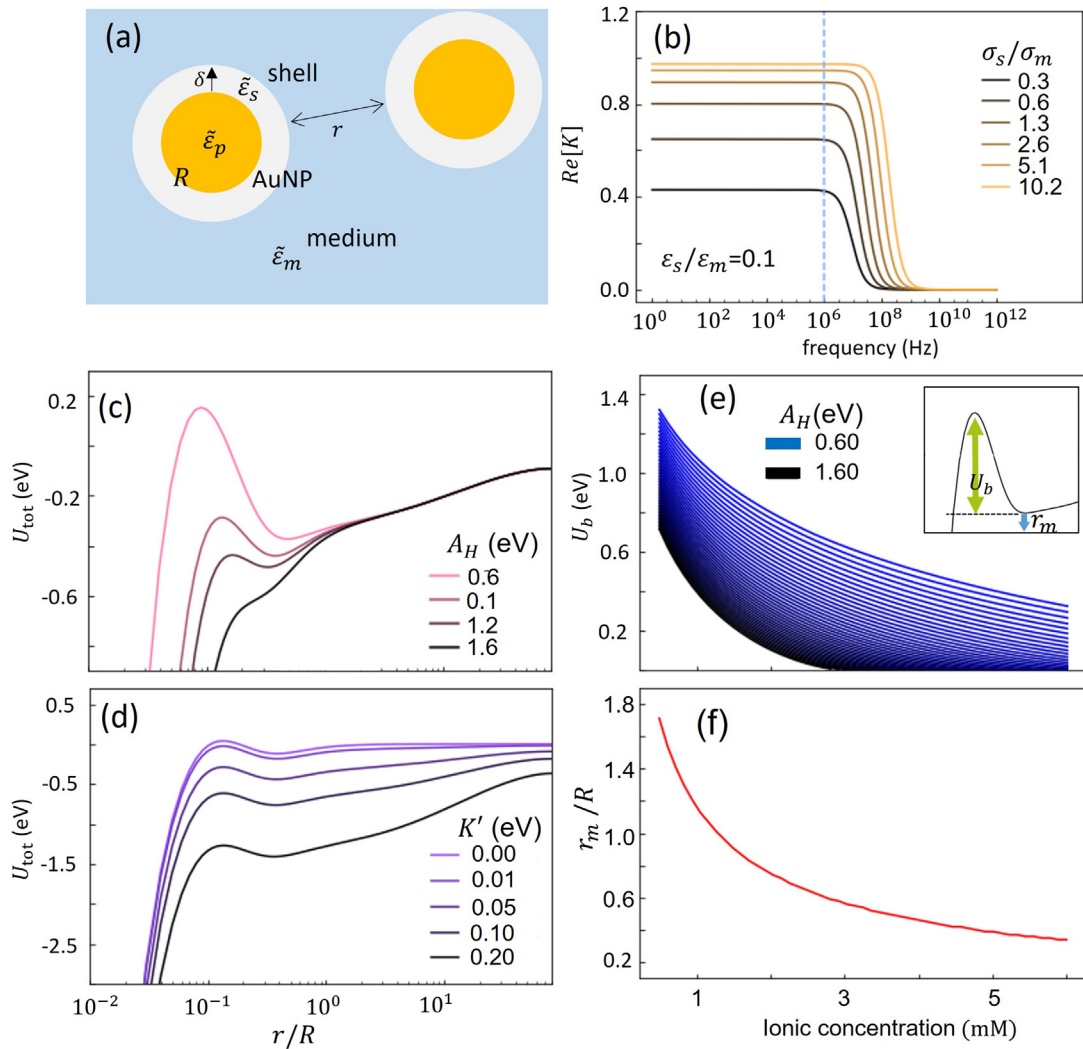
FIG. 4. (a) Composite model for AuNP with an ionic shell suspended in the liquid medium. (b) Real part of the Clausius–Mossotti factor Re(K') for the shell model with $\sigma_m = 228 \mu$S/cm setting the transition frequency from Eq. (4). (c) Total potential at 3.8 mM for varying A_H (K' = 0.05) or (d) varying K', $A_H = 1$ eV. (e) Barrier height (defined in inset) and (f) position of local minimum vs ionic strength. For all cases $\zeta = -54$ mV (measured with Zetasizer Nano, Malvern Panalytical), $\varepsilon_m = 79$, $V_p = 20$ V.

$$K' = \frac{\tilde{\varepsilon}'_p - \tilde{\varepsilon}_m}{\tilde{\varepsilon}'_p + 2\tilde{\varepsilon}_m} = \frac{h\tilde{\varepsilon}_s - \tilde{\varepsilon}_m}{h\tilde{\varepsilon}_s + 2\tilde{\varepsilon}_m}$$

with modified MW transition frequency at   (4)

$$\omega'_{MW} = \frac{\sigma'_p + 2\sigma_m}{\varepsilon'_p + 2\varepsilon_m}.$$

Given the frequency dependence arising from the lower conductivity shell σ_s, this now reduces the DEP force starting around the MHz region [Fig. 4(b)], since the shell can no longer respond fast enough.

With measured medium conductivity $\sim$200 μS/cm (equivalent to 4 mM citrate ions), the Debye length $\lambda_D \sim 5$ nm is taken as the shell thickness δ. The electric field distribution is analytically approximated as that from two symmetrical hyperbolic 2D conductors,[24] allowing the total potential to be extracted for different separations of NPs [Figs. 4(c) and 4(d)]. This reveals that an extra secondary minimum appears where the NPs do not come into contact but remain separated by distances on the order of their diameter. The barrier height remains above 25 meV, ensuring that permanent aggregation does not occur in this regime at room temperature.

The conductivity of the medium is an important parameter in our model and is fixed while V, f are scanned in these experiments. We also qualitatively test our model for two additional conductivities: one lower and one higher than the $\sim$200 μS/cm of our NP batches. In the first case, the colloidal gold nanoparticles are centrifuged and the supernatant replaced by DI water, reducing the ion concentration and decreasing the medium conductivity. The AuNP-cloud then forms at slightly lower frequencies $\sim$1 MHz, which cannot be achieved using the original conductivity colloid solution. This is compatible with our prediction that lower medium conductivities give lower transition frequencies ω'_{MW} [Eq. (4)]. In the second case, a 100 μl droplet of CB[5] (cucurbit[5]uril, 100 μ M) is added to the nanoparticle solution, which increases the conductivity of the liquid medium by $\sim$5% (measured with Zetasizer Nano, Malvern Panalytical). AuNP-cloud formation is then shifted to higher frequencies, above 5 MHz. We, however, note that modifications of the ion concentration can also change the AuNP colloid stability.

The main factors reducing the barrier height to irreversible contact are increasing the Hamaker factor [Fig. 4(c)] and ionic strength [Fig. 4(e)], which increases the NP attraction and reduces the shell size. On the other hand, the double-layer shell stabilizes this secondary minimum [Fig. 4(d)]. The stable cloud formation (as well as reversible NP concentration near electrodes), thus, results from the reduced U_{DEP} at MHz frequencies, which prevents the attraction of AuNPs to the electrodes and to each other. It results in a cloud with average NP center-to-center separations of $\sim$ 200 nm and, thus, saturates the NP density in the cloud. This matches fairly well with the observed estimated NP separations of $\sim$1 μm but still does not account for some features such as the cloud formation in the middle of the gap even though the field density gradient is smaller here. We suggest that the screening ions are not uniformly distributed in different gap regions with lower ion densities in the center giving larger shells around NPs, in turn producing larger barriers U_b and larger stable separations r_m [Figs. 4(e) and 4(f)].

The presence of dense NPs with double-layer shells inside the gap should alter the capacitance of the solution and, thus, also be electrically measurable. However, current measurements of V_s are dominated by the conductivity of the entire solution, and cloud formation is not easily seen from this signal because although it is predicted to increase by $\sim$ 0.5%, rf electrical noise means this is at the detection limit. Improvements in electrical probing architectures should enable feedback of the trapping process entirely electrically.

The dynamic structure of the trapped AuNP cloud remains to be discovered. A periodic array of NPs would be expected to produce photonic crystal scattering-based structural color;[25] however, on 100 ms timescales of spectral measurement here, this was not observed. This suggests that polycrystalline domains must change rapidly, and the structure remains effectively amorphous, though this might still be expected to develop color from the short-range correlations. Dynamic light scattering in different geometries will be useful to probe this but suffers currently from strong backgrounds due to the electrode edges and surfaces.

The accumulation of particles can modify the local electric field and change the dynamics of AuNP-cloud formation, opening up future directions to study the time evolution of this 3D system. Our model explains the reversibility of trapping, in contrast to permanent attachment of particles leading to chain formation, but suggests more complex dynamics can appear. How nanoparticles are trapped near the middle of the gap and away from the high field gradient electrode edges is not clear, but we now suggest a possible mechanism to direct future studies. In equilibrium, the cluster of nanoparticles in the AuNP-cloud holds its shape under strong mutual dipole–dipole interactions. This may arise from dynamic chain formation, their subsequent anisotropic motion, and then their breaking near the cloud edges. Such internal motions should be detectable.

The successful trapping of AuNPs in reversible potentials demonstrated here opens up domains to explore for nanoassembly. Because the trapping can continue at the same time as a (gentle) flow of the solution, the surrounding AuNP solution can be replaced leaving only the trapped NPs in position. Additional linker molecules can then be flowed in to "cross-link" the NP structure. The nascent understanding presented here shows how NP separation can be controlled by the rf frequency and ion concentration [Fig. 4(f)]. This suggests that the dynamic NP lattice can be gradually condensed (in the presence of short linker molecules) to develop unusual types of NP lattice structures and, thus, useful nanodevices such as sensors. Previous irreversible kinetically trapped aggregate structures can, thus, instead now be accessed in quasi-equilibrium, allowing annealing to reach stable target organized nanostructures.

In summary, reversible aggregation and formation of concentrated clouds of AuNP clusters within electrode gaps are demonstrated using MHz dielectrophoresis. A frequency resonance of the trapped NP density seen in the dark-field scattering intensity is found at $\sim$ 2 MHz for 20 V rf modulation. A theoretical model combining DLVO theory for colloids with the effect of the dielectrophoretic potential on the double-layer surrounding AuNPs suggests how such a resonance can occur in the MHz domain. The self-aligned trapping of AuNPs near electrical contacts in a controllable manner offers the prospect of well-defined scalable routes to nanodevice construction.

AUTHOR DECLARATIONS
Conflict of Interest

The authors have no conflicts to disclose.

DATA AVAILABILITY

The data that support the findings of this study are openly available at DOI 10.17863/CAM.84363.

REFERENCES

[1]B. Sarno, D. Heineck, M. J. Heller, and S. D. Ibsen, Electrophoresis **42**, 539 (2021).

[2]R. Pethig, Biomicrofluidics **4**, 022811 (2010).

[3]L. Zheng, J. P. Brody, and P. J. Burke, Biosens. Bioelectron. **20**, 606 (2004).

[4]K. D. Hermanson, S. O. Lumsdon, J. P. Williams, E. W. Kaler, and O. D. Velev, Science **294**, 1082 (2001).

[5]K. H. Bhatt and O. D. Velev, Langmuir **20**, 467 (2004).

[6]R. Kretschmer and W. Fritzsche, Langmuir **20**, 11797 (2004).

[7]S.-H. Cha, S.-H. Kang, Y. J. Lee, J.-H. Kim, E.-Y. Ahn, Y. Park, and S. Cho, Sci. Rep. **9**, 3629 (2019).

[8]K. Fu, S. Chen, J. Zhao, and B. G. Willis, ACS Sens. **1**, 444 (2016).

[9]S. Cherukulappurath, S. H. Lee, A. Campos, C. L. Haynes, and S. H. Oh, Chem. Mater. **26**, 2445 (2014).

[10]A. Barik, L. M. Otto, D. Yoo, J. Jose, T. W. Johnson, and S. H. Oh, Nano Lett. **14**, 2006 (2014).

[11]B. C. Gierhart, D. G. Howitt, S. J. Chen, R. L. Smith, and S. D. Collins, Langmuir **23**, 12450 (2007).

[12]A. Nerowski, M. Poetschke, M. Bobeth, J. Opitz, and G. Cuniberti, Langmuir **28**, 7498 (2012).

[13]S. Park and A. Beskok, Anal. Chem. **80**, 2832 (2008).

[14]P. Bahukudumbi, W. N. Everett, A. Beskok, M. A. Bevan, G. H. Huff, D. Lagoudas, and Z. Ounaies, Appl. Phys. Lett. **90**, 224102 (2007).

[15]A. Henning-Knechtel, M. Wiens, M. Lakatos, A. Heerwig, F. Ostermaier, N. Haufe, and M. Mertig, Beilstein J. Nanotechnol. **7**, 948 (2016).

[16]M. H. V. Werts, F. Allix, O. Francais, C. Frochot, L. Griscom, B. Le Pioufle, M. Loumaigne, and J. Midelet, IEEE J. Sel. Top. Quantum Electron. **20**, 6900613 (2014).

[17]H. Morgan and N. G. Green, *AC Electrokinetics: Colloids and Nanoparticles* (Research Studies Press, 2003).

[18]A. Ramos, P. García-Sánchez, and H. Morgan, Curr. Opin. Colloid Interface Sci. **24**, 79 (2016).

[19]T. Kim, K. Lee, M. S. Gong, and S. W. Joo, Langmuir **21**, 9524 (2005).

[20]E. J. W. Verwey and J. T. G. Overbeek, *Theory of the Stability of Lyophobic Colloids: The Interaction of Sol Particles Having an Electric Double Layer* (Elsevier Publishing Company, 1948).

[21]A. Ramos, H. Morgan, N. G. Green, and A. Castellanos, J. Colloid Interface Sci. **217**, 420 (1999).

[22]A. Ramos, H. Morgan, N. G. Green, and A. Castellanos, J. Phys. D **31**, 2338 (1998).

[23]T. B. Jones, *Electromechanics of Particles* (Cambridge University Press, 1995).

[24]J. Lekner, Eur. J. Phys. **25**, 737 (2004).

[25]A. I. Haines, C. E. Finlayson, D. R. E. Snoswell, P. Spahn, G. P. Hellmann, and J. J. Baumberg, Adv. Mater. **24**, OP305 (2012).